

## Bulk-like Emission in the Visible Spectrum of Colloidal $\text{LiYF}_4\text{:Pr}$ Nanocrystals Downsized to 10nm

Rajesh Kombar<sup>‡\*</sup>, Simon Spelthann<sup>‡\*</sup>, Michael Steinke, Detlev Ristau, Axel Ruehl, Christoph Gimmmler\* and Horst Weller

<sup>‡</sup> Authors contributed equally to this work

\* Corresponding authors

### Experimental section:

#### *Chemicals and materials:*

Hydrated chloride of yttrium (99.9%) was purchased from Treibacher and that of praseodymium (99.9%) from Sigma Aldrich. Lithium hydroxide (99.995%) monohydrate, ammonium fluoride (99.99%), and toluene (99.8%) were procured from Sigma-Aldrich. Technical grade oleic acid and octadecene were acquired from Alfa Aesar.

#### *Synthesis of $\text{LiYF}_4\text{:Pr}$ nanocrystals:*

Syntheses of  $\text{LiYF}_4$  nanocrystals doped with upconverting ions have been reported elsewhere.<sup>1</sup> Here, the synthesis of  $\text{LiYF}_4\text{:Pr}$  NC was conducted in a Schlenk-line set up with some modifications. For the synthesis of 3 mmol nanocrystals of  $\text{LiYF}_4\text{:Pr}$  (0.65, 1, 1.3, and 1.5 at%), an appropriate amount of rare earth chlorides (yttrium and praseodymium) in methanol were mixed with 20 ml oleic acid and 20 ml octadecene in a 50 ml three necked round bottom flask which was connected to a reflux condenser, temperature sensor, and septum. At first, the mixture was heated to 170 °C for 30 min under stirring and nitrogen atmosphere and was cooled down again to 50 °C. Then the mixture was degassed at 100 °C under vacuum, should be less than 1 mbar, to remove volatiles. After that, 3 mmol (0.126 g) lithium hydroxide was added under nitrogen flow and stirred under vacuum for another 30 min. Thereafter, 12 mmol (0.444 g) ammonium fluoride was added to the mixture. The mixture was then heated to 300 °C under nitrogen atmosphere for 90 Min. After cooling down to below 30 °C the solution was precipitated with 1:1 addition of ethanol and collected by centrifugation (7000 g). The residue was redispersed in 10 ml toluene and the washing step was repeated if necessary. Finally, the precipitated nanocrystals were redispersed in 5 ml toluene.

#### *Synthesis of 5% $\text{Pr}^{3+}$ doped $\text{LiYF}_4$ nanocrystals:*

The same synthesis procedure were adopted by varying appropriate amount of yttrium and praseodymium chlorides.

#### *Size tuning of 5% $\text{Pr}^{3+}$ doped $\text{LiYF}_4$ nanocrystals:*

Particle sizes of 15 nm and 20 nm were achieved by varying LiOH content to 2 mmol/mmol and 3 mmol/mmol respectively. All the other parameters were kept unchanged.

#### *XRD, TEM, and EDX Characterizations:*

XRD analysis was done in a PANalytical X'PERT Pro diffractometer with a  $\text{Cu K}\alpha$  X-ray source (0.154 nm) and the samples were prepared on Si wafer. For that 50  $\mu\text{L}$  of the obtained stable colloidal dispersions containing nanocrystals was directly dried on a Si wafer. A JEOL JEM-1011 operating on 100 kV was used for capturing TEM images. 10  $\mu\text{L}$  of the diluted colloidal solution was used as samples solution, which then dried on the copper grid for TEM analysis. The incorporated  $\text{Pr}^{3+}$  ions in the nanocrystals were analysed using an energy dispersive X-ray technique (EDX) coupled to a TEM (Jeol JEM 2200 FS; FEG cathode, 200 kV, Oxford X-Max 100TLE, SDD 100  $\text{mm}^2$ ). At least three different areas on the TEM grids were irradiated with electron beam and spontaneously ejected X-rays captured by the detector were used for analysing the elemental content of the nanocrystals.

Experimental set up and measurement procedure for lifetime, emission, absorption and absorption cross section fitting analyses are provided below in the supporting information.

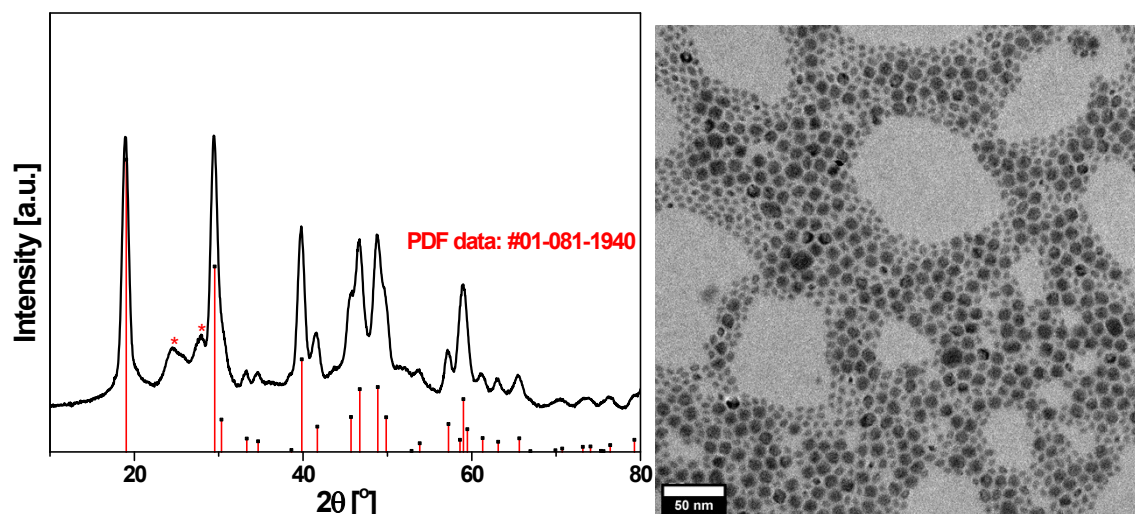


**Figure S1:** left) XRD of  $\text{LiYF}_4$ :1 at% Pr nanocrystals is plotted along with corresponding PDF data (#01-081-1940) of tetragonal  $\text{LiYF}_4$  and presence of the other phase (YF<sub>3</sub>) are marked; right) respective TEM; shows polydisperse particles.

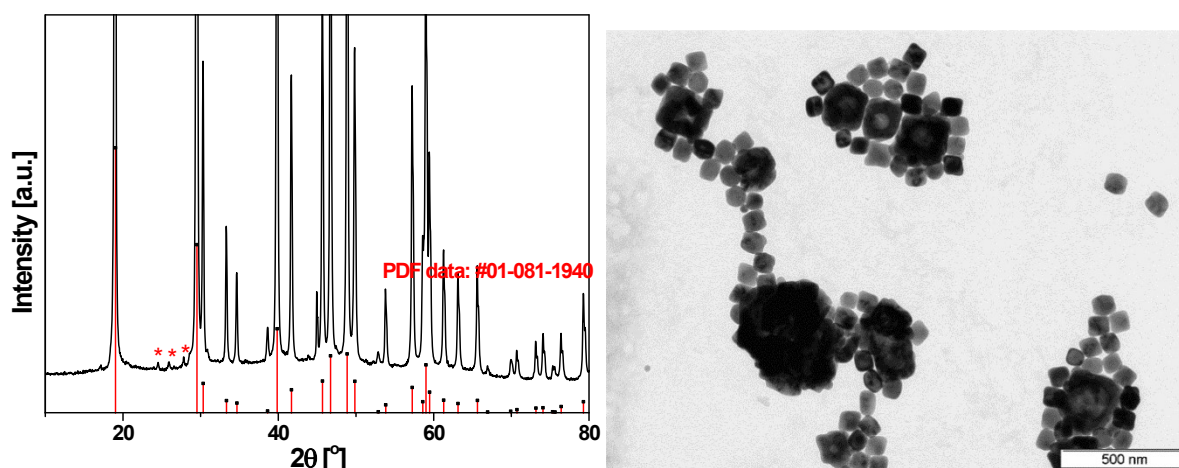


**Figure S2:** left) XRD of  $\text{LiYF}_4$ :1 at% Pr nanocrystals prepared with less oleic acid is plotted along with corresponding PDF data (#01-081-1940) of tetragonal  $\text{LiYF}_4$  and presence of the other phase are marked; right) respective TEM; shows polydisperse particles of  $\text{LiYF}_4$ :1 at% Pr nanocrystals; size is increased, but not monodisperse.

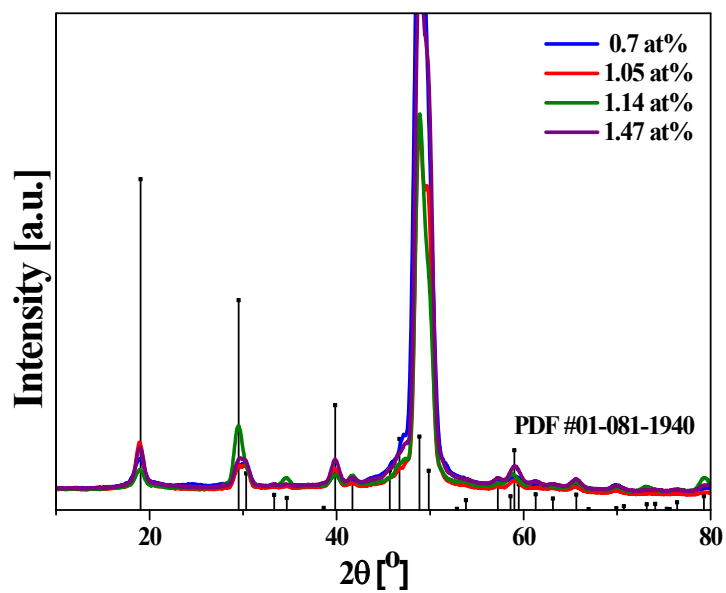


**Figure S3:** XRD of LiYF<sub>4</sub>:x at% Pr nanocrystals and is plotted along with corresponding PDF data (#01-081-1940) of tetragonal LiYF<sub>4</sub>

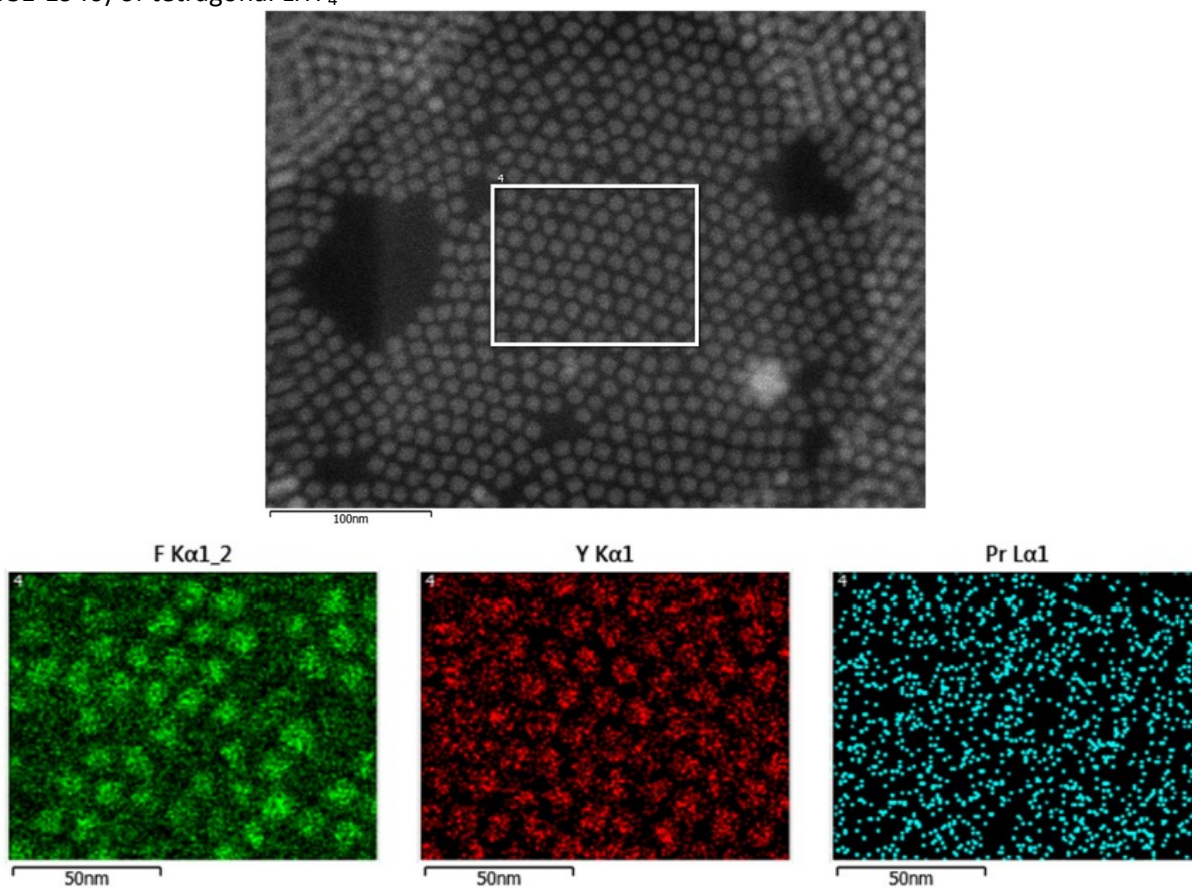


**Figure S4a:** Mapping of LiYF<sub>4</sub>:x 1,47% Pr nanocrystal, above: mapped area; below: mapped atoms from left to right F, Y and Pr.

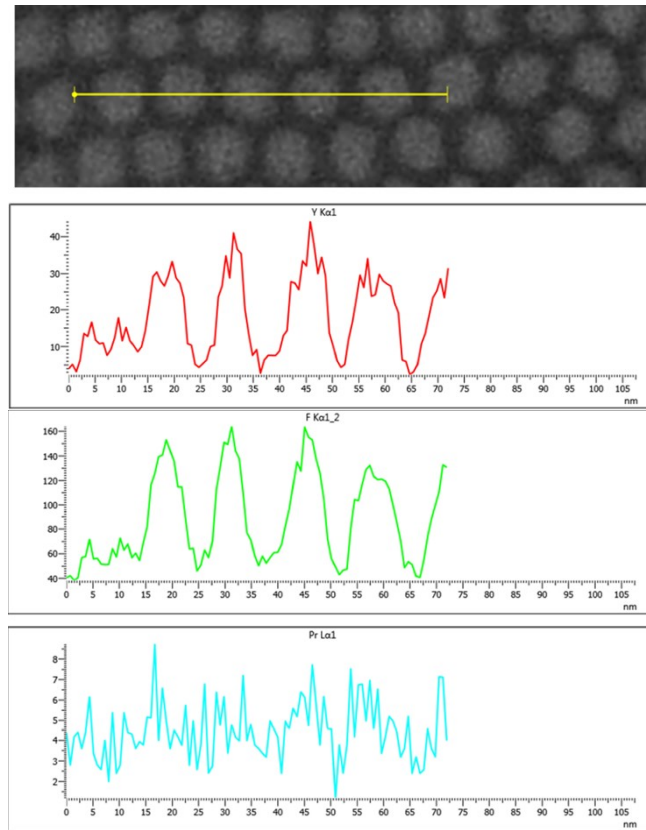


**Figure S4b:** Line scan of  $\text{LiYF}_4:x$  1,47% Pr nanocrystal, from top to bottom: line scanned area; line scanned data of Y, F and Pr.

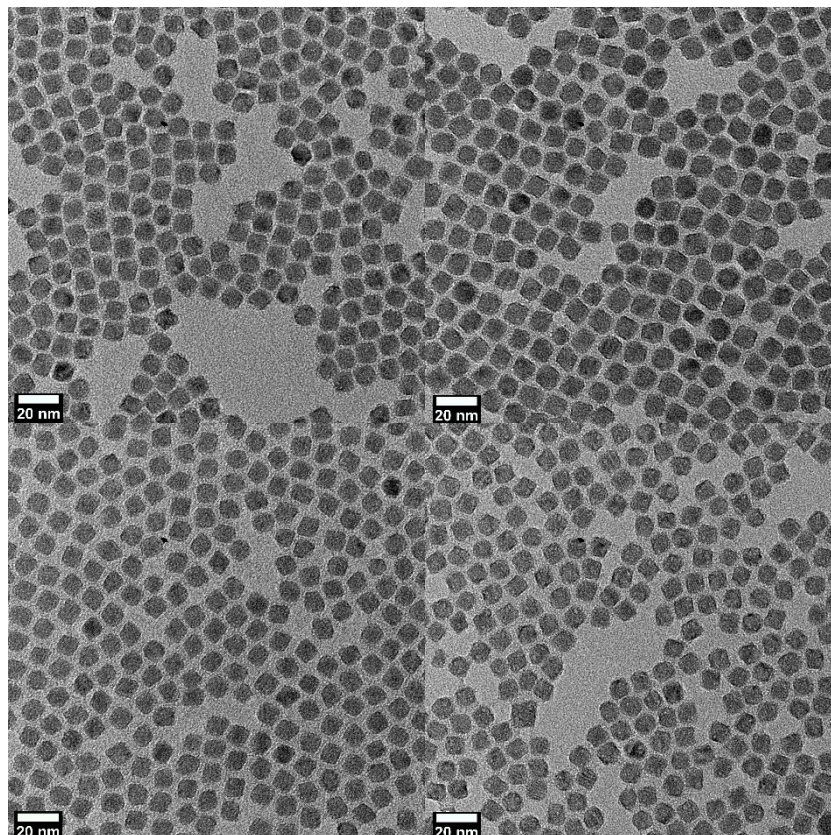


**Figure S5:** TEM of  $\text{LiYF}_4:x \text{ at\% Pr}$  nanocrystals [above: left) 0.7 at% and right) 1.05 at%; below: left) 1.14 at% and right) 1.47 at%] with the tetragonal bipyramidal morphology of NCs visible.

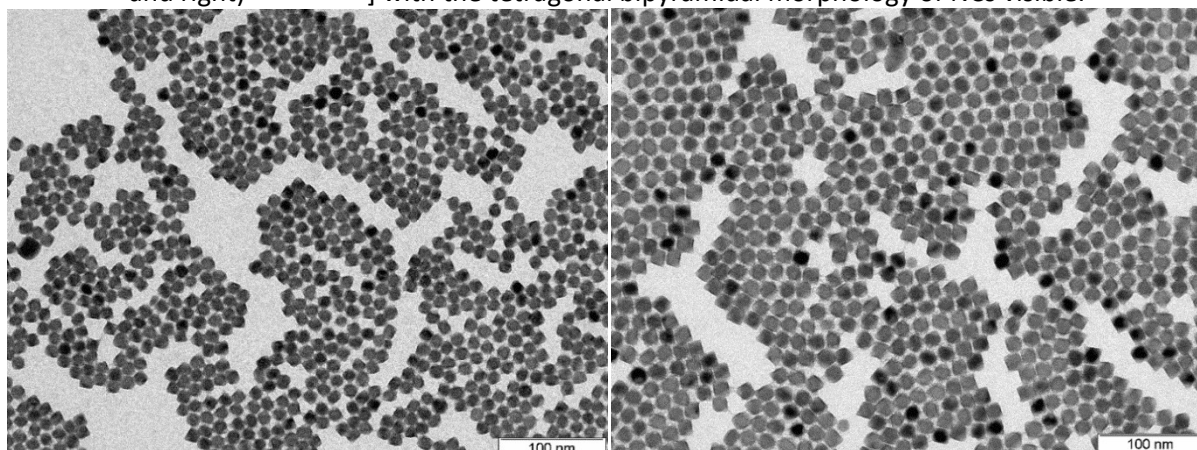


**Figure S6:** TEM analysis of  $\text{LiYF}_4:\text{Pr}$  nanocrystals with (5%)  $\text{Pr}^{3+}$  concentration: a) 15 nm b) 20 nm

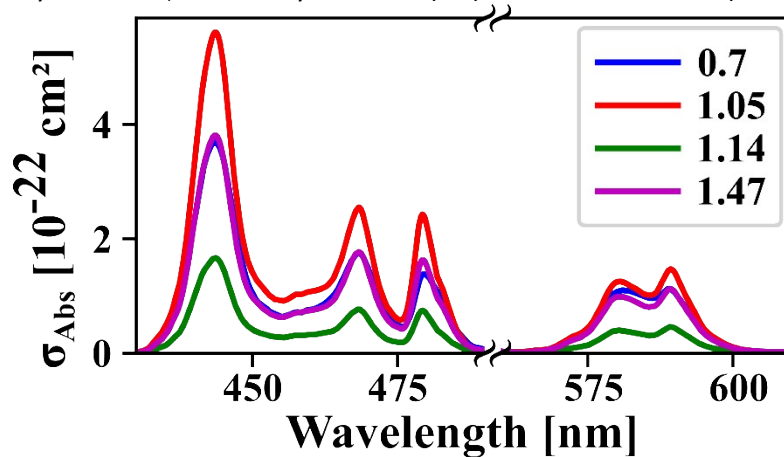


**Figure S7:** Absorption cross sections  $\text{LiYF}_4:x \text{ at\% Pr}$  nanocrystals (blue: 0.7 at%, red: 1.05 at%, green: 1.14 at%, magenta: 1.47 at%).

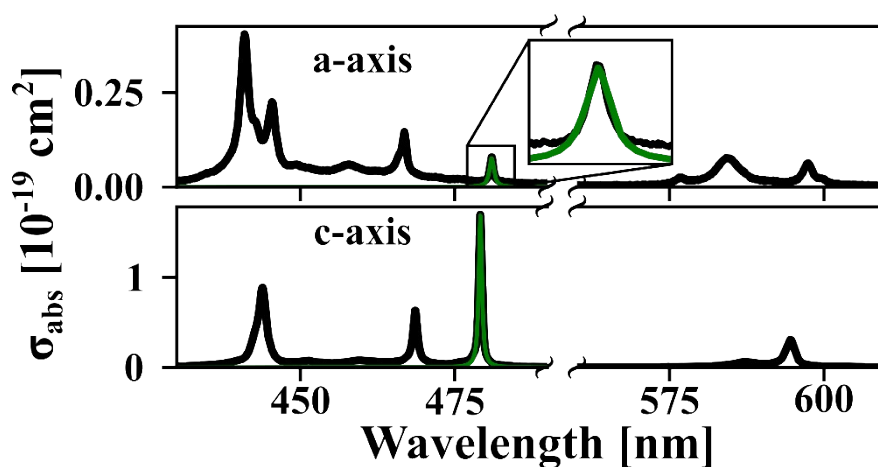


**Figure S8:** Absorption cross sections of  $\text{LiYF}_4:0.65 \text{ at\% Pr}$  bulk crystal and exemplary fit of a Lorentzian-profile to the peak corresponding to the  ${}^3\text{H}_4 \rightarrow {}^3\text{P}_0$  transition.

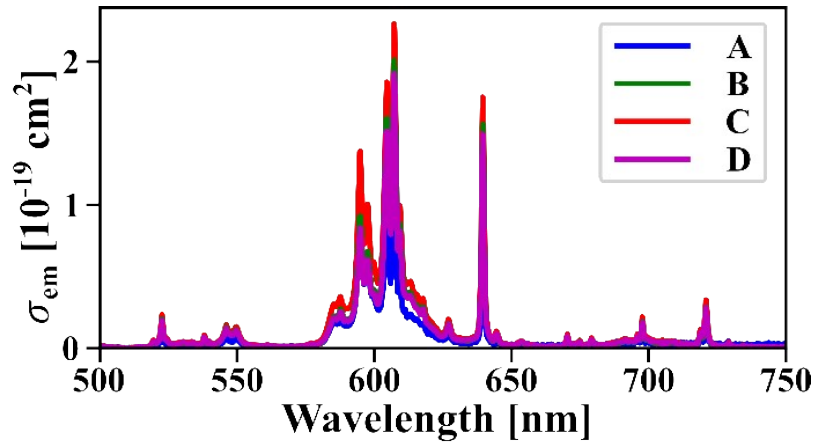


**Figure S9:** Emission cross sections LiYF<sub>4</sub>:x at% Pr nanocrystals (blue: 0.7 at%, red: 1.05 at%, green: 1.14 at%, magenta: 1.47 at%).

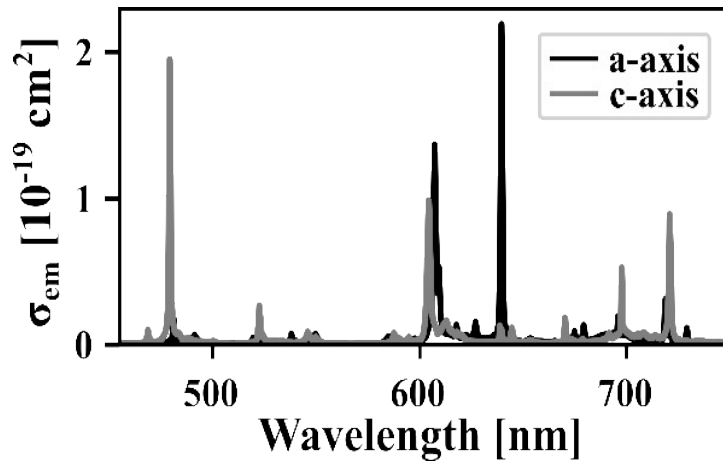


**Figure S10:** Emission cross sections of a bulk crystal.

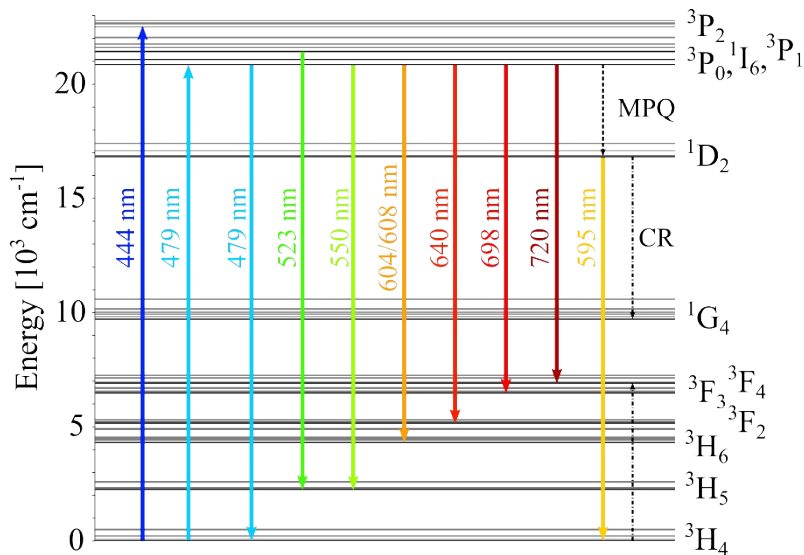


**Figure S11:** Energy level diagram of LiYF:Pr<sup>3+</sup> with all relevant transitions in the visible spectrum. Multiphonon Quenching (MPQ) from the <sup>3</sup>P<sub>0</sub> level leads to population of the <sup>1</sup>D<sub>2</sub> level. Cross relaxation (CR) reduces the lifetime of the <sup>1</sup>D<sub>2</sub> level for high numbers of Pr<sup>3+</sup> ions in the nanocrystals.

### Lifetime measurement procedure and experimental set up

The  $\text{LiYF}_4:\text{Pr}$  nanocrystal dispersions were filled into cuvettes with a length of  $l_{opt} = 1 \text{ cm}$ . These cuvettes were used to measure the dynamics and spectrum of the spontaneous emission as well as the absorption. A sketch of the setup used for the measurement of the spontaneous emission dynamics is depicted below (**Figure S12**).

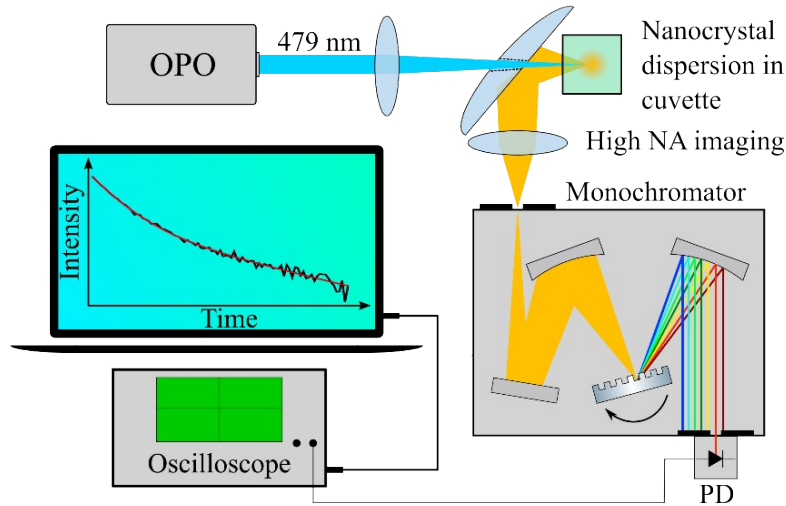


**Figure S12:** Experimental Setup for the measurement of the excited state lifetime.

An optical parametric oscillator (OPO, Spectra Physics ULD-240) tuned to  $479 \text{ nm}$  was used to excite the nanocrystals from the ground state  $^3\text{H}_4$  to the  $^3\text{P}_0$  state. A maximum excitation energy of  $5 \text{ mJ}$  at a pulse duration of  $5 \text{ ns}$  was used to obtain sufficient signal to record the spontaneous emission decay. The OPO radiation was focused into the cuvette using a lens with  $500 \text{ mm}$  focal length. A parabolic mirror was used to collect emission from the nanocrystals. The collected light was focused to a monochromator using high numerical aperture (NA) lenses. The monochromator was tuned to the emission wavelength of interest. A  $100 \text{ MHz}$  Si-photodiode (Femto OE-300-SI) with integrated gain module has been used to detect the emission dynamics. The pump pulses cannot be resolved with this setup as the photodiode's response time limits the resolution to  $10 \text{ ns}$ . The photodiode was connected to a  $0.5 \text{ GHz}$  oscilloscope (Tektronix 620B) with a sampling rate of  $2.5 \text{ GSa/s}$  terminated by a  $50 \Omega$  resistor. This oscilloscope was connected to a computer for data collection. An average of  $100$  measurements was sufficient to reduce noise and eliminate the influence of energy fluctuations of the OPO pulses. Despite the monochromator acting as a filtering element to the emitted light a fast component was detected in the temporal signal which corresponded to residual excitation light. Using optical long pass filters and housing of the beam paths the residual excitation light was strongly reduced, however, not fully removed.

Thus, the measured decay dynamic traces result from a superposition of three different signals. The first one arises from the residual pump light, which is not properly filtered from the optical signal and has no physical meaning. The second contribution is the emission of the nanocrystals. This signal is superimposed with emission from the organic ligands. Both of these signals are expected to have time constants about three orders of magnitude higher than the signal of the pump signal.

To extract the two time constants of the decay from the nanocrystals a bi-exponential fitting procedure was applied. Before that, the original trace was corrected by the noise at the beginning and the end of the data. Then, a region of interest (ROI) was selected as shown in **Figure S13** to cut out insignificant data such as parts of the baseline without signal and especially the residual pump signal. The ROI is set by cutting the decay signal between the time stamps  $t_1$  and  $t_2$ . The initial time stamp  $t_1$  is used to cut the pump signal while the final time stamp  $t_2$  marks the point where the signal approaches the baseline

noise. Furthermore, a moving average filter to smoothen the data was investigated to reduce the signal noise.

A bi-exponential function in the form

$$y(t) = y_0 + a \cdot \exp\left(-\frac{t}{\tau_1}\right) + b \cdot \exp\left(-\frac{t}{\tau_2}\right)$$

was fitted to the ROI. One of the exponential functions represents the decay of the organic ligands emission while the other one represents the decay of the spontaneous emission originating from the nanocrystals. Preliminary investigations on oleic acid showed that the time constant of this decay is in the order of some microseconds. From bulk crystals it is known that the excited state lifetime of the nanocrystals may range in the order of some tens of microseconds. Therefore, the higher time constants can be allocated to the nanocrystals response.

To ensure the independence of the obtained time constants from the choice of fitting parameters, we performed in a first step an extensive analysis of the influence of the initial time stamp  $t_1$ . Bi-exponential fits were applied for a varying length of the initial time stamp. The results are depicted in **Figure S14** and **Figure S15** for  $^3P_0$  and  $^1D_2$  emission, respectively. Due to the presence of the residual pump light in the decay signal it is expected that the obtained time constant strongly depends on the choice of  $t_1$  within the first microseconds followed by a plateau where the obtained lifetime is independent on the choice of  $t_1$ . This is clearly the case for all samples.

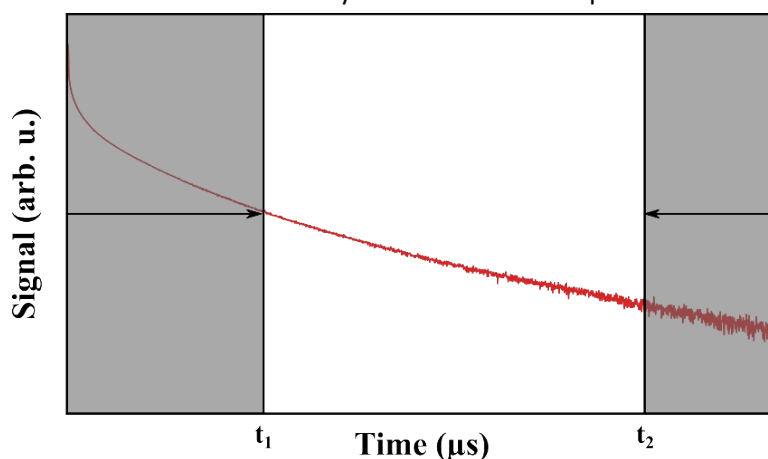


**Figure S13:** Schematic of the cutting of the region-of-interest.

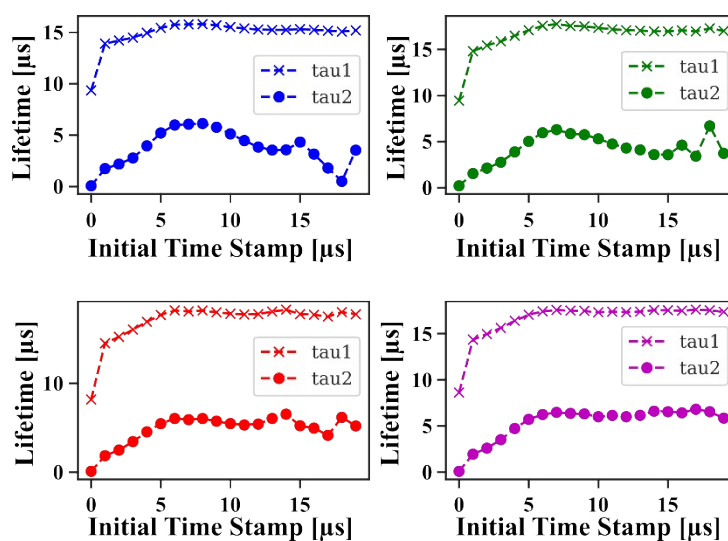


**Figure S14:** Dependence of the fit result of the excited state lifetimes of the  $^3P_0$  level for  $\text{LiYF}_4:x$  at%  $\text{Pr}^{3+}$  nanocrystals on the initial time stamp (blue: 0.7 at%, red: 1.05 at%, green: 1.14 at%, magenta: 1.47 at%).

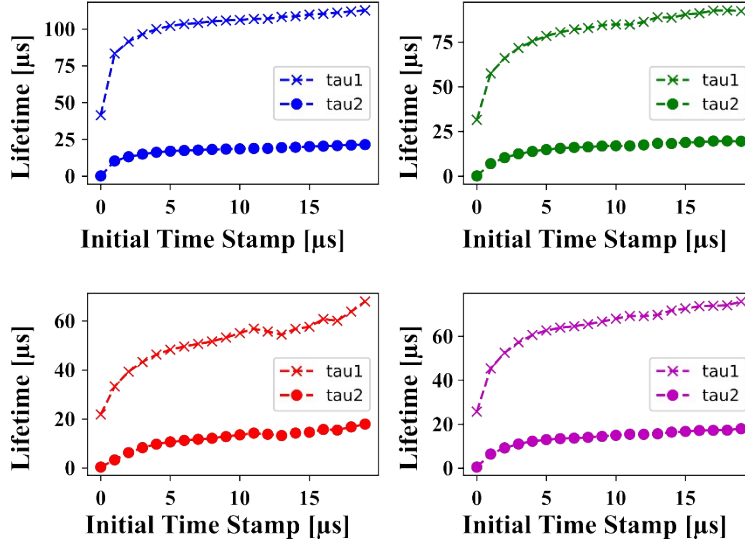


**Figure S15:** Dependence of the fit result of the excited state lifetimes of the  $^1D_2$  level for  $\text{LiYF}_4:x$  at%  $\text{Pr}^{3+}$  nanocrystals on the initial time stamp (blue: 0.7 at%, red: 1.05 at%, green: 1.14 at%, magenta: 1.47 at%).

For every sample, an individual time stamp  $t_1$  was set to 5  $\mu\text{s}$ . A comprehensive investigation on the second time stamp  $t_2$  was not needed as this time stamp was easily determinable from the noise level of the raw data. The lifetimes were obtained by calculating the arithmetic mean of the fitted lifetimes from 5  $\mu\text{s}$  to the end of the curves in Figure S14 and 15, respectively. The lifetimes are presented in **Figure 4** in the main text.

#### Estimation of the nonradiative rate

The nonradiative to radiative rates ratio can be obtained from the quantum yield  $\eta$ . The nonradiative rate is represented by  $1 - \eta$ . Thus, the ratio can be estimated via  $(1 - \eta)/\eta$ .

#### Emission spectroscopy:

The emission spectra presented in the paper were obtained using the same laser source and setup as described above. The spontaneous emission was separated from the excitation light using a long-pass filter at 500 nm. Then it was coupled to an optical multimode fiber which was connected to an USB-spectrometer (RGB Photonics QWave) with a spectral resolution of 0.42 nm.

To determine the quantum yield, absorption and emission spectra were obtained from an absolute photoluminescence spectrometer (Edinburgh Instruments FLS 1000) with an integrated integration sphere at a spectral resolution of 1 nm. First, excitation and emission spectra  $S_0^{exc}(\lambda)$  and  $S_0^{em}(\lambda)$  of toluene filled cuvettes were recorded in the respective spectral range. Next, both spectra  $S^{exc}(\lambda)$  and  $S^{em}(\lambda)$  were measured for the nanocrystal dispersions. The quantum yield was obtained from these spectra via

$$\phi = \frac{\int_{exc} S^{exc}(\lambda) d\lambda - \int_{exc} S_0^{exc}(\lambda) d\lambda}{\int_{em} S^{em}(\lambda) d\lambda - \int_{em} S_0^{em}(\lambda) d\lambda}$$

Here, not only the  $^3P_0$  but also the  $^3P_2$  level was addressed by setting the excitation wavelength to 444 nm.

### Absorption spectroscopy

The transmission was measured with a UV/VIS/NIR photospectrometer (Perkin Elmer Lambda 1050) with a resolution of 0.05 nm. First, a baseline was recorded with a cuvette containing just the organic solvent. Next, the dispersions were measured. In the last step, this measurement was corrected by the baseline.

The raw transmission spectra show discrete peaks which can be assigned to the well-known absorption lines of Pr ions. Furthermore, a broad sigmoid-like absorption can be observed. This absorption can be assigned to the oleic acid (OA) ligands around the nanocrystals. These ligands may oxidize during the synthesis. This process leads to a red-shift of the absorption acting like a bandgap as depicted in Figure S8. The high oxidation state of OA was obtained by heating at 300 °C for two hours under influence of oxygen.

OA also shows an emission characteristic which intensifies with the oxidation state. Comparing Figure S8 to Figure 2D in the paper reveals a very low oxidation state of the ligands in the samples presented as there is no underground visible in the emission spectra.

The absorption spectrum of the oleic acid was subtracted from the transmission  $T$ . Due to the very small particle size which is around a factor of 50 smaller than the wavelength scattering is assumed to be negligible. Lambert-Beer's law was applied to the transmission data

$$I(\lambda, z) = I_0 \exp(-\alpha z)$$

$$T = \frac{I(\lambda, z)}{I_0}$$

with the transmission  $T = \frac{I(\lambda, z)}{I_0}$ . The propagation parameter  $z$  was set to the cuvette length  $l$  in the present case and the absorption coefficient  $\alpha$  was determined. The ion density  $N$  was determined from the nanocrystal data so that the absorption cross sections were obtained from

$$\sigma_{abs} = \frac{\alpha(\lambda)}{N}$$

The resulting absorption cross sections for every sample investigated in this work is depicted in Figure S4. These cross sections differ by roughly 50 % which has to be attributed to inaccuracies in the size distribution analysis as well as the EDX analysis. Typically, one would expect the same cross sections for doping concentrations as low as investigated in this work.

Emission cross sections were obtained applying the Füchtbauer-Ladenburg equation

$$\sigma_{em} = \frac{1}{8\pi c n^2 \tau} \cdot \frac{\lambda^5 I(\lambda)}{\Sigma I(\lambda) \lambda d\lambda}$$

Here,  $c$  is the speed of light,  $n$  the refractive index  $\tau$  the excited state lifetime, and  $I$  the intensity of the emission. The refractive index was obtained from Maxwell-Garnets effective medium theory<sup>2</sup> and the excited state lifetime was obtained from the measurements described in this paper.

The resulting emission cross sections are depicted in Figure S6. These cross sections only differ by a few percent which is expected. Again, the inaccuracies have to be attributed to inaccuracies within the measurements and analysis. Emission cross sections of a bulk crystals are depicted in Figure S7.

### Absorption Cross Sections Fitting

Absorption cross sections of the bulk crystals are well described with a Lorentzian-profile as depicted in Figure S5 representing homogenous broadening mechanisms. However, fitting each individual transition in both bulk and nanocrystal absorption and comparing them is not promising as such fit is heavily overdetermined. Therefore, another approach was chosen to quantify the spectral changes of the absorption cross sections. The mechanism influencing the absorption of the nanocrystals can be both, homogenous and inhomogeneous.

A combination of homogenous and inhomogeneous broadening mechanisms can be described by a convolution of Lorentzian- and Gaussian-profile, respectively, represented by the so-called Voigt-profile  $V$

$$V(\lambda, A, \lambda_c, \sigma, \gamma) = \frac{A \cdot \text{Re}[w(z)]}{\sigma \cdot \sqrt{2\pi}}$$

where

$$z = \frac{\lambda - \lambda_c + i\gamma}{\sigma\sqrt{2}}$$

$$w(z) = e^{-z^2} \cdot \text{erfc}(-iz)$$

and  $f(x) = \text{erfc}(x)$  is the complementary error function. Furthermore,  $A$ ,  $\lambda_c$ ,  $\sigma$ , and  $\gamma$  are the amplitude, central wavelength of the peak, standard deviation of the Gaussian part, and the scale parameter, which specifies the half-width at half-maximum of the Lorentzian part, respectively.

It is assumed that there are two classes of ions: ions which are fully affected and ions that are not at all affected by the mechanism which leads to the spectral changes. Fitting the broadening and shift of each transition individually, would over-determine the fit. Therefore, we chose a global fitting approach, assuming that all energy levels are affected equally. As the convolutions are associative it is now sufficient to convolve a single Voigt-profile with a weighted sum of the bulk absorption spectra for both axes. The weight factor was also set as fit parameter. In the fitting procedure, one global spectral shift for both spectra is allowed. Furthermore, a non-broadened part is included in the fit function to account for the not-affected ions. Using a Voigt-profile accounts for both homogenous and inhomogeneous broadening mechanisms.

Such fit was performed for all absorption spectra with comparable results. Therefore, only the results on the 1.47 mol% doped sample are discussed in the paper.

Besides this discussion, it can be seen from the results that the assumptions made for this fitting procedure are not precisely correct as the peak at 468 nm is not well fitted. The fit discussed in the paper also contains some inaccuracies at the peaks around 479 nm and 444 nm, respectively. This indicates that the broadening mechanism does not affect all transition in the same way. From the energy level scheme, it can be seen that this absorption band results from a superposition of transitions from the ground state  $^3H_4$  to either the  $^1I_6$  or the  $^3P_1$  level. These two levels are coupled and thus might not behave equally to the  $^3P_2$  and  $^3P_0$  level. Nevertheless, applying a global fitting routine is sufficient for a qualitative discussion regarding the broadening mechanisms.

#### Literature

- 1 F. Wang, J. Wang, Y. Xu, Y. Wang, Y. Liu, X. Chen, H. Chen and X. Liu, *Comptes rendus Chimie*, 2010, **13**, 731
- 2 K. Dolgaleva, R.W. Boyd, and P. W. Milonni, *J. Opt. Soc. Am. B.*, 2007, **24**, 516.